ECS Transactions, 68 (1) 1499-1508 (2015)
10.1149/06801.1499ecst ©The Electrochemical Society

Screen Printed Porous $La_{0.20}Sr_{0.25}Ca_{0.45}TiO_3$ Fuel Electrode Scaffold Microstructures: Optimisation of Interaction with Impregnated Catalysts for More Durable Performance

R. Price[a], M. Cassidy[a], J. A. Schuler[b], A. Mai[b] and J. T. S. Irvine[a]

[a] School of Chemistry, University of St Andrews, St Andrews, Fife, KY16 9ST, UK
[b] Hexis AG, Zum Park 5, CH-8404 Winterthur, Switzerland

$La_{0.20}Sr_{0.25}Ca_{0.45}TiO_3$ ($LSCT_{A-}$) shows promise as a novel Solid Oxide Fuel Cell anode backbone material (to replace Ni-based cermets). Thick film ceramic processing techniques have been used as the primary method in controlling the characteristics of the fuel electrode (layer thickness, porosity, grain connectivity and the ultimate interaction with catalyst particles) in order to produce a microstructural architecture which has the potential to deliver higher electronic (and ionic) conductivity, improved current distribution and more durable performance in fuel cell testing. Results of preliminary studies into the ceramic processing of $LSCT_{A-}$ are presented here.

Introduction

Solid Oxide Fuel Cells (SOFCs) are energy conversion devices which allow externally-fed fuel gases, e.g. H_2 or CH_4, to be electrochemically oxidized for the efficient production of electricity and heat (1). Unlike other fuel cells, SOFCs contain a solid, oxide anion conducting electrolyte material, meaning that the entire cell is comprised of solid materials (2) and must be operated at temperatures between 600 and 1000 °C to ensure ionic conduction takes place (3). This makes them particularly suitable for the role of combined heat and power (CHP) generation in family homes.

The current industrial standard SOFC anode material is the Ni-based cermet (Ni-YSZ or Ni-CGO). Although it shows excellent catalytic activity for the electrochemical oxidation (direct or steam reforming) of hydrocarbons, it is intolerant of coke formation and sulphur poisoning (1) and has the potential to exhibit redox instability (especially in anode-supported cells) (4). Therefore, a new anode material which removes these problematic properties would be advantageous.

Recent research has shown that the infiltration of catalyst materials onto supporting skeletal backbones holds great promise as a potential route to overcome the issues mentioned above (5). A promising new material which may be used as a 'backbone' for a SOFC anode layer has been identified. $La_{0.20}Sr_{0.25}Ca_{0.45}TiO_3$ ($LSCT_{A-}$) is a A-site deficient perovskite pertaining to the $SrTiO_3$ family of perovskites. The bulk material has previously been shown to exhibit a high electronic conductivity under reducing conditions (27.53 S cm^{-1}) (6) and anode layers of $LSCT_{A-}$ impregnated with 10 wt. % CeO_2 and 5 wt. % NiO have delivered high initial performances during testing with the fuel cell manufacturer: Hexis AG, Switzerland (7).

However, in research previously carried out by Verbraeken *et al*., thin anodes layers of 12-15 μm and inadequate microstructures of the $LSCT_{A-}$ backbone led to the formation of localised temperature 'hotspots' and poor current distribution in short-stack (5 cells) and full-scale (60 cells) testing. The result of full-scale testing in the Hexis Galileo 1000N 1 kW (nominal) micro combined heat and power unit was degradation of power output from ~700 W to ~250 W after only 600 hours of testing (7).

As this impregnated material shows high catalytic activity for the oxidation of methane, and resulted in a high initial power output during full-scale testing, it is necessary to carry out further research in order to reduce the observed degradation significantly. Thus, optimisation of the anode backbone layer is required to obtain a suitable thickness, porosity, grain connectivity (leading to high lateral conductivity) and impregnability for electrocatalytic particles.

Experimental

Cell Fabrication

Electrolyte Preparation. The tape-casting method was primarily used to create electrolytes. A tape-casting slurry was produced in a three-step process (8). Firstly, 8YSZ (8 mol % yttria-stabilised zirconia, 0.5 - 0.7 μm, Daiichi Kigenso Kagaku Kogyo Co. Ltd.), distilled water, Hypermer KD6 dispersant (uniqema) and a defoaming agent (WT001, Polymer Innovations) were roller ball milled for 20 hours. Subsequently, the plasticisers: polyethylene glycol (average M_W: 300, Sigma-Aldrich) and glycerol (Alfa Aesar) were added, followed by a binder consisting of 15 wt % polyvinyl alcohol (High M_W, Alfa Aesar) in distilled water and extra defoaming agent. The resultant mixture was roller ball milled at reduced speed for 4 hours before degassing at very low speed for a further 20 hours. Tapes were laminated, cut and then fired at 1400 °C to produce planar electrolytes ~18 mm in diameter.

Anode Ink Formulation. $La_{0.20}Sr_{0.25}Ca_{0.45}TiO_3$ powder (Treibacher Industrie AG, Austria), terpineol (anhydrous, mixture of isomers, Sigma-Aldrich) and Hypermer KD1 Dispersant (Uniqema) in terpineol were planetary ball milled for two hours. Then, a polyvinyl butyral binder (PVB) (Butvar, Sigma-Aldrich) in terpineol was mixed in using the same method at a reduced milling speed for 30 minutes.

Screen Printing and Sintering. The resultant ink was used to screen print 1 cm^2 anodes onto the 8YSZ electrolytes (DEK248 semi-automatic screen printer). Both 325 and 230 mesh screens (MCI Precision) were used to print anode layers, with each screen requiring different numbers of prints to achieve the same thickness of anode. The resultant anodes were fired at a range of firing temperatures and dwell times to give rise to a variation in microstructure.

Impregnation

Precursor solutions of the electrocatalyst impregnates were prepared by separately dissolving $Ce(NO_3)_3.6H_2O$ (99 %, Sigma-Aldrich), $Ni(NO_3)_2.6H_2O$ (99 %, Acros Organics), $Cu(NO_3)_2.3H_2O$ (99 – 104 %, Sigma-Aldrich), $Fe(NO_3)_3.9H_2O$ (≥98 %,

Sigma-Aldrich) and $Mn(NO_3)_2.6H_2O$ (>98 %, Alfa Aesar) in ethanol, whilst $Ru(NO_3)_3(NO)$ in nitric acid was used as supplied (Johnson Matthey). Nitric acid was added to $Cu(NO_3)_2.3H_2O$ and $Mn(NO_3)_2.6H_2O$ solutions in order to promote dissolution of the solids. The nitrate solutions were used to impregnate the anode 'backbone' structure before being decomposed at 500°C to form the electrocatalytic particles.

Characterisation

The 'backbone' and impregnated anode microstructures were examined using a Jeol JSM 6700F FEG-SEM; porosity and thickness measurements were carried out on the SEM images using ImageJ; rheometric analysis of the anode inks was undertaken using a Brookfield DV-III Ultra Rheometer, equipped with a small sample spindle (SC4-14), and particle size analysis was carried out using a Malvern Instruments Mastersizer 2000.

Results and Discussion

Physical Properties of Powder and Inks

Optimisation of the overall solids loading, through alteration of the dispersant, binder and solvent loadings, was targeted first, in order to improve the printability of the $LSCT_{A-}$ ink. A series of screen printing inks were produced, ranging from 62 % to 81 % solids loading. It was determined that inks of >75 % $LSCT_{A-}$ loading could not be successfully de-agglomerated or suspended in the terpineol solvent. As a result, a range of inks spanning 62 % to 75 % solids loading were characterised by analysis of rheology and particle size distribution. During rheological analysis, the variation of shear stress as a function of shear rate was fitted to the form of a power law behaviour and flow indices (a measure of the degree of variation from Newtonian flow) were obtained as a result. Particle size distribution data allowed determination of D_{50} values (the particle size below which 50 % of the particles lie). Table I summarises the flow indices and D_{50} values of each ink (including raw $LSCT_{A-}$ powder for comparison).

TABLE I. Rheometric flow indices and particle size distribution data for the $LSCT_{A-}$ inks created.

Solids ($LSCT_{A-}$) Loading of Ink/%	Flow Index/a.u.	D_{50}/µm
62	1.00	1.66
65	1.00	1.69
67	0.98	2.01
70	0.98	1.77
72	0.95	1.67
75	0.80	1.53
$LSCT_{A-}$ Powder *	-	1.74

*** $LSCT_{A-}$ powder was dispersed in distilled water whereas inks were dispersed in isopropyl alcohol (IPA).**

As higher solids loadings of $LSCT_{A-}$ were reached, the suspensions became gradually less Newtonian, indicated by the decreasing value of flow index. Whilst ink formulations lying between the 62 % and 72 % solids loading may still be called Newtonian-like fluids (with flow indices are close to unity), the largest and most significant departure from Newtonian behaviour is seen at 75 % solids loading. The corresponding plots of shear stress against shear rate are shown in Figure 1.

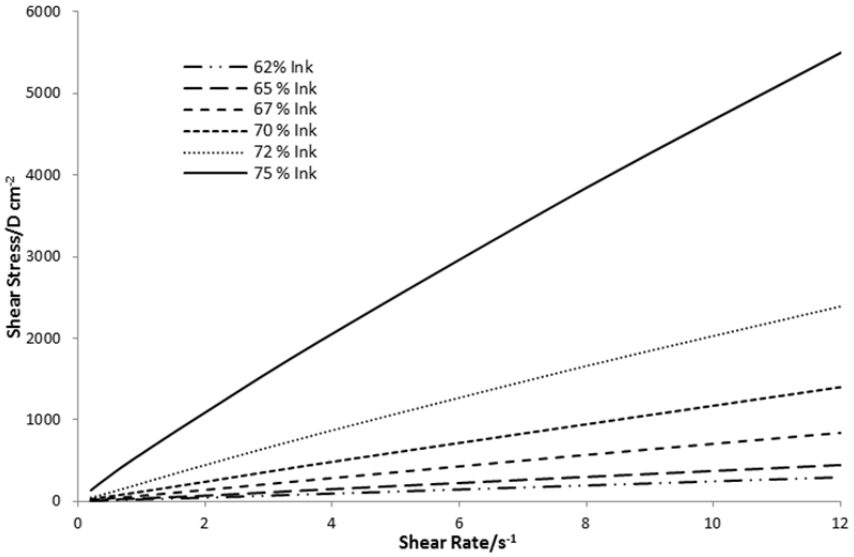

Figure 1. Plot of shear stress against shear rate for all solids loadings of $LSCT_A$- inks produced.

The flow index of 0.80 (for the 75 % solids loading ink) implies pseudo-plasticity, resulting in the exhibition of shear-thinning behaviour; a reduction in viscosity upon application of shear stress (9). This is ideal for the screen printing process as the viscous ink employed will exhibit a temporary drop in viscosity on application of shear stress (i.e. the movement of the squeegee over the screen). This allows the ink to flow through the porous area of the screen, onto an electrolyte, and flow laterally to remove any mesh marks that may have resulted. Subsequently, original viscosity is restored with time after the application of stress to prevent lateral ink leakage and loss of desired geometry (10). Figure 2 shows the non-linear plot of shear stress vs. shear rate for the 75 % solids loading $LSCT_A$- ink formulation, in particular. Figure 2 also shows that the down-scan data does not deviate from the up-scan data. This indicates that no thixotropic behavior (time-dependent shear-thinning) is exhibited by this ink: a further useful characteristic for screen printing inks which prevents them from spreading out laterally over longer time periods after the deposition of the anode layer.

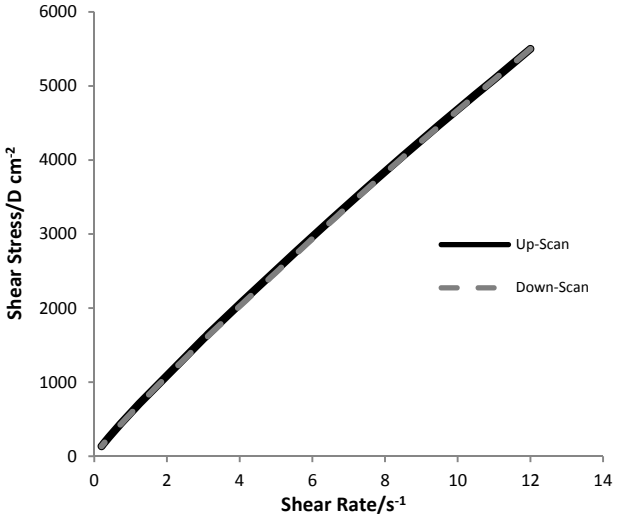

Figure 2. Plot of shear stress against shear rate showing the pseudo-plastic behaviour of the 75 % solids loading ink.

For particle size analysis, the raw $LSCT_{A-}$ powder was dispersed in distilled water, whilst the inks were dispersed in IPA as it is used as a standard ink solvent. Table I shows that $LSCT_{A-}$ powder exhibited a D_{50} value of 1.74 μm, whilst the SEM image (Figure 3) suggested a particle size of 1-2 μm. In comparison to this, the $LSCT_{A-}$ particles were well dispersed in all of the inks with the 75 % ink exhibiting the best dispersion with D_{50} = 1.53 μm, due to the action of the Hypermer KD1 dispersant.

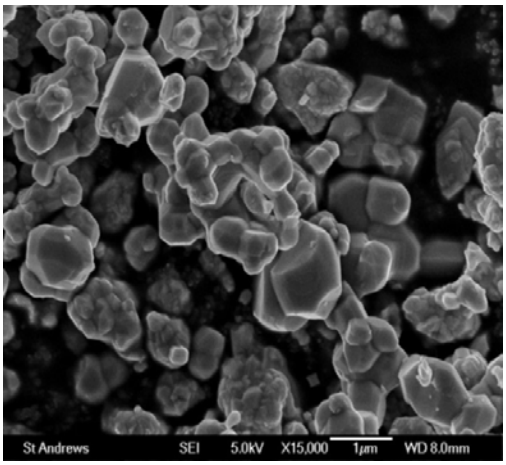

Figure 3. A scanning electron micrograph of the $LSCT_{A-}$ powder (as received) with a particle size of 1-2 μm.

Effect of Screen Printing on Microstructure

Due to the homogeneity and pseudo-plasticity pertaining to the 75 % solids loading ink (hereafter referred to as LSCT75), this formulation was selected for screen printing trials. Thicker anode layers of optimised porosity and grain connectivity were produced in order to accommodate better current distribution and the lateral conductivity of the layers. Two screens were employed in screen printing of anode layers: a 325 mesh count (per inch) screen and a 230 mesh screen. The former provides a much smaller open porosity for the ink to flow through which, when combined with a finer wire, gives a thinner screen and thinner deposited layer, in comparison to the latter. This meant that different numbers of prints were required to achieve the desired overall thickness upon sintering (at least 50 μm).

Printing of LSCT75 with the 325 mesh screen deposited 15-20 μm green ink layers in one cycle, hence 5 cycles were required to achieve an appropriate thickness. The resultant cells were sintered at different temperatures and dwell times. Table II summarises the sintering protocol, resultant anode thickness and porosity.

TABLE II. Details of sintering protocol and final physical parameters for screen printed anode layers of LSCT75 (with a 325 mesh screen).

Sintering Temperature/°C	Dwell Time/hours	Anode Thickness/μm	Porosity/%
1250	1	76	50.5
1250	2	76	45.4
1275	1	98	45.9
1275	2	79	42.4
1300	1	80	43.7
1300	2	80	42.2

Figure 4 shows the SEM images used to extract the data in table II. A significant difference in porosity (~5 %) between the sample sintered at 1250°C for 1 hour (1250 °C/1h) and the samples sintered at higher temperature and/or dwell times was seen. The 50.5% porosity of this sample implies that it may not provide enough grain connectivity to allow sufficient lateral conductivity. This also implies that a temperature of 1250°C and dwell time of at least 2 hours is required to obtain a microstructure that may begin to be considered suitable for application as a SOFC fuel electrode. Overall, the porosity generally decreased as expected with increasing temperature and dwell time, although some fluctuations in porosity were observed (e.g. sample 1300°C/1h had a higher porosity than sample 1275°C/2h). This shows that the combination of sintering temperature and dwell time is important in controlling the porosity and microstructure of the anode layer. Sample 1300°C/2h showed the smallest porosity of the samples, however, it also displayed the most suitable combination of grain connectivity and porosity for a 'backbone' or anode scaffold.

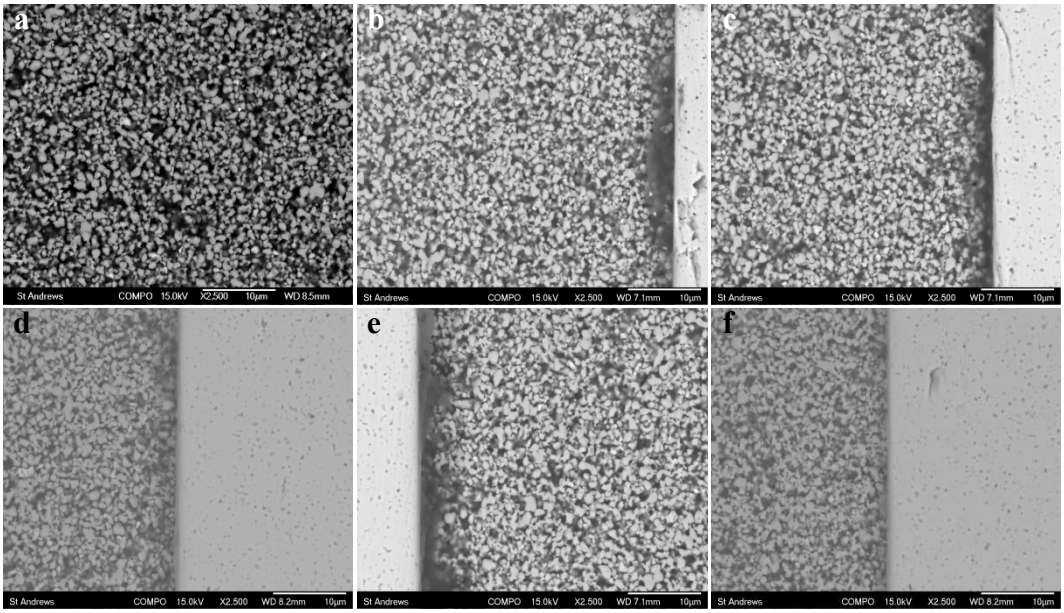

Figure 4. SEM images of the fuel electrode 'backbone' microstructures (screen printed with a 325 mesh screen) for samples sintered at: a) 1250°C/1h, b) 1250°C/2h, c) 1275°C/1h, d) 1275°C/2h, e) 1300°C/1h and f) 1300°C/2h.

Subsequently, screen printing of anode layers using a 230 mesh screen was investigated to determine the effect on the scaffold microstructure. Due to the increased thickness of the screen, resulting from the larger open porosity and the thicker wires, thicker printed layers were expected. So, a series of 3 prints was sufficient (in the majority of samples) to produce a layer thickness in excess of 50 µm after sintering. Identical sintering protocol was employed, allowing direct comparison of the two sets of microstructures. The physical properties of these anode layers are summarised in table III.

TABLE III. Details of sintering protocol and final physical parameters for screen printed anode layers of LSCT75 (with a 230 mesh screen).

Sintering Temperature/°C	Dwell Time/hours	Anode Thickness/µm	Porosity/%
1250	1	69	52.7
1250	2	47	46.8
1275	1	64	48.9
1275	2	78	47.3
1300	1	77	47.1
1300	2	74	45.7

The larger open porosity of this screen would have caused a change in the rheology of the ink. A larger aperture reduces the shear stress that the ink experiences as it passes through the screen. This means that a lower viscosity drop is experienced by the ink when using the 230 mesh screen compared to using the 325 mesh screen (which has a lower open porosity and exerts a higher shear stress on the ink as it flows through). This implies that the ink returns to its equilibrium viscosity more quickly (11), with the 230 mesh screen, and gives $LSCT_{A-}$ particles less time to rearrange leading to slightly less dense packing arrangement in the 'green' body of the anode layer. This may account for the larger porosity values seen in Figure 5 compared with those in Figure 4, after sintering.

Figure 5 shows the SEM images of the resultant microstructures (to which the data in table III belong). As expected, the general trend of decreasing porosity with temperature/dwell time was conserved. The images show that a similar style of grain connectivity and porosity is present in the scaffold microstructures of the anodes produced with the 325 and 230 mesh screens. However, the sample sintered at 1300 °C/2h, with the 230 mesh screen, clearly shows a much better developed grain connectivity, whilst retaining a high porosity, compared to all other samples.

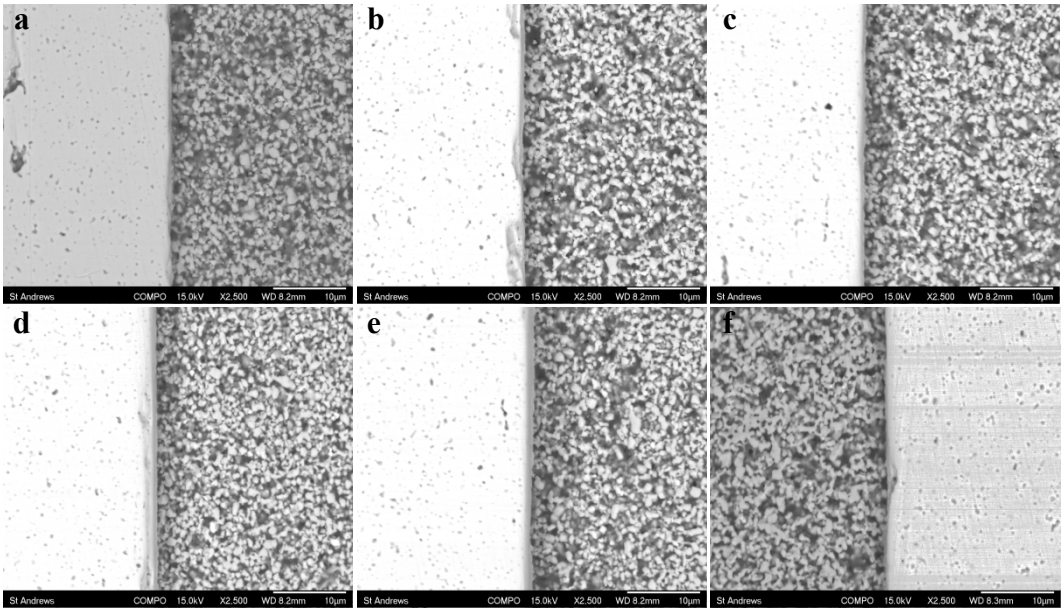

Figure 5. SEM images of the fuel electrode 'backbone' microstructures (screen printed with a 230 mesh screen) for samples sintered at: a) 1250 °C/1h, b) 1250 °C/2h, c) 1275 °C/1h, d) 1275 °C/2h, e) 1300 °C/1h and f) 1300 °C/2h.

Impregnation of Microstructures

As the anode layer printed with the 230 mesh screen and fired at 1300°C for 2 hours appeared to give the best combination of porosity and grain connectivity, it was selected for impregnation studies. Presented below are initial results in the form of SEM images (Figure 6) of post-impregnation microstructures and the accompanying porosity data (Table IV). Nitrate solutions of Ce, Cu, Fe, Mn and Ni (10 wt % of anticipated oxide) and the nitrosyl nitrate solution of Ru (5 wt % of anticipated oxide) were impregnated into separate anode layers and decomposed at 500°C.

TABLE IV. Details of post-impregnation microstructural porosity for screen printed anode layers of LSCT75 (with a 230 mesh screen) sintered at 1300 °C/2h.

Impregnated Solution	Post-Impregnation Porosity/%
$Ce(NO_3)_3.6H_2O$	40.1
$Cu(NO_3)_2.3H_2O$	44.0
$Fe(NO_3)_3.9H_2O$	35.9
$Mn(NO_3)_2.6H_2O$	38.2
$Ni(NO_3)_2.6H_2O$	44.1
$Ru(NO_3)_3(NO)$	38.6

The data in table IV show that there is a reduction in porosity of the microstructure after impregnation for each impregnate. However, the reduction in porosity is much more apparent for species such as the anticipated Fe and Mn oxides. Though, for species which form particles upon reduction, the porosity may increase again. This must be a consideration when designing the final electrode microstructure, as too dense an anode will result in poor gas diffusion and mass transport losses.

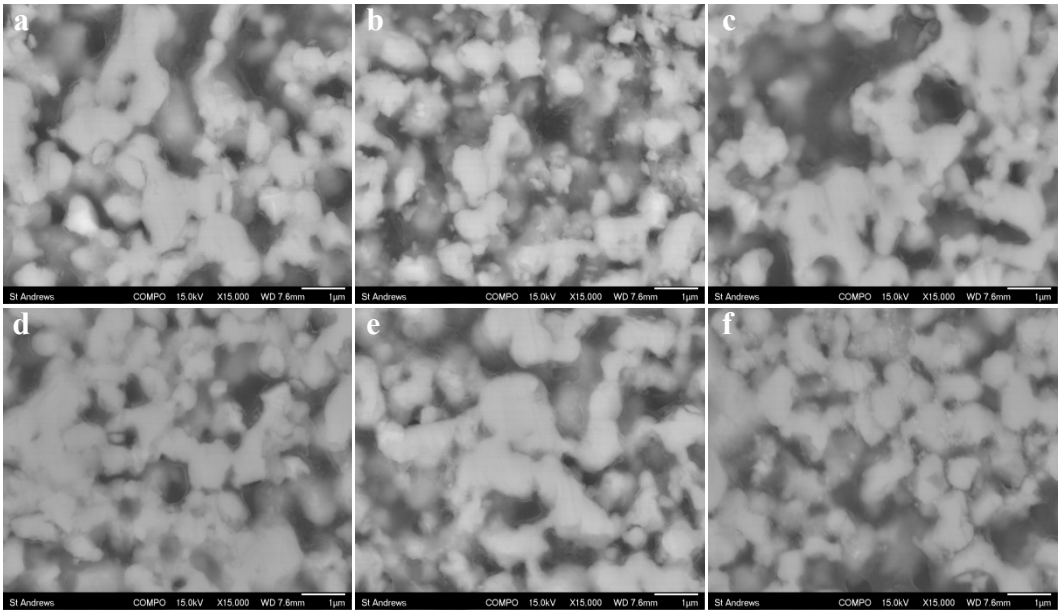

Figure 6. SEM images of fuel electrode 'backbone' microstructures screen printed with a 230 mesh screen and sintered at 1300°C/2h, followed by impregnation with: a) $Ce(NO_3)_3.6H_2O$, b) $Cu(NO_3)_2.3H_2O$, c) $Fe(NO_3)_3.9H_2O$, d) $Mn(NO_3)_2.6H_2O$, e) $Ni(NO_3)_2.6H_2O$ and f) $Ru(NO_3)_3(NO)$.

Figure 6 illustrates fuel electrode scaffold microstructures which have been impregnated with different transition/lanthanide metal nitrate solutions. A 'particle-coating' (the impregnates) can be seen on the backbone microstructures which has led to the partial densification of the anode. Furthermore, in Figures 6 b and 6 f, it is already possible to see small particles of impregnates at the surface of grains, even before reduction. These may be metal particles or the oxides of Cu and Ru, respectively.

Conclusion

Initial results obtained in the study of thick film ceramic processing techniques on the fuel electrode scaffold microstructures of $LSCT_A$- show that the screen mesh count and open porosity employed during screen printing have a significant effect on the microstructure produced upon sintering. From the range of microstructures presented, only the anode layer produced with the 230 mesh screen and sintered at 1300 °C for 2 hours shows an adequate combination of porosity and grain connectivity. This microstructure allows efficient impregnation of transition/lanthanide metal/metal oxide precursor solutions leading to a series of 'coated' microstructures of varying porosity, sometimes bearing impregnate particles. This final porosity must be carefully controlled to retain a sufficient pore volume for diffusion of reactant and product gases. Future work will include energy dispersive analysis of X-rays (EDAX) of the impregnated samples, as well as conductivity testing to confirm the optimised microstructures in terms of grain connectivity and the magnitude of change in conductivity upon impregnation with the previously discussed impregnates.

Acknowledgments

We would like to thank Hexis AG and the University of St Andrews for financial support. Thanks also go to Dr Cristian Savaniu and Dr Maarten Verbraeken for their assistance in facilitating research.

References

1. C. Sun and U. Stimming, *J. Power Sources*, **171**, 247 (2007).
2. P. Holtappels and U. Stimming, in *Handbook of Fuel Cells – Fundamentals, Technology and Applications*, W. Vielstich, A. Lamm and H. A. Gasteiger, Editors, p. 335, John Wiley & Sons, Chichester (2003).
3. J. H. Hirschenhofer, D. B. Stauffer, R. R. Engleman and M. G. Klett, *Fuel Cell Handbook*, 4th ed., p1-4, Parsons Corporation, Philadelphia (1998).
4. S. P. Jiang, *Mater. Sci. Eng. A*, **418**, 199 (2006).
5. M. Cassidy, G. Lindsay and K. Kendall, *J. Power Sources*, **61**, 189 – 192 (1996).
6. A. D. Aljaberi and J. T. S. Irvine, *J. Mater. Chem. A*, **1**, 5868 (2013).
7. M. C. Verbraeken, B. Iwanschitz, E. Stefan, M. Cassidy, U. Weissen, A. Mai and J. T. S. Irvine, in *11th European SOFC and SOE Forum*, A0905, P. 1 – 13, Lucerne (2014).
8. M. C. Verbraeken, M. Cassidy and J. T. S. Irvine, in *Advances in Solid Oxide Fuel Cells 9*, N. P. Narottram, M. Kusnezoff, S. Kirihara and S. Widijada, Editors, p. 67, John Wiley & Sons, New Jersey (2013).

9. R. Mistler and E. Twiname, *Tape Casting: Theory and Practice*, p. 272, The American Ceramic Society, Westerville, Ohio (2000).
10. C. B. Carter and M. G. Norton, *Ceramic Materials*, 2nd ed., p. 503, Springer New York, New York (2013).
11. J. Savage, in *Handbook of Thick Film Technology*, P. J. Holmes and R. G. Loasby, Editors, p. 56, Electrochemical Publications Ltd., Port Erin, Isle of Man, British Isles (1976).